Terphenyl-based Small-Molecule Inhibitors of Programmed Cell Death-1/Programmed Death-Ligand 1 Protein−Protein Interaction

Damian Muszak[1], Ewa Surmiak[1*], Jacek Plewka[2], Katarzyna Magiera-Mularz[1], Justyna Kocik[1], Bogdan Musielak[1], Dominik Sala[1], Radosław Kitel[1], Malgorzata Stec[3], Maciej Siedlar[3], Alexander Dömling[4], Lukasz Skalniak[1], Tad A Holak[1*]

[1]Department of Organic Chemistry, Faculty of Chemistry, Jagiellonian University, Gronostajowa 2, 30-387 Krakow, Poland

[2]Malopolska Centre of Biotechnology, Jagiellonian University, Gronostajowa 7a, 30-387 Kraków, Poland

[3]Department of Clinical Immunology, Institute of Pediatrics, Jagiellonian University Medical College, Wielicka 265, 30-663 Krakow, Poland

[4]University of Groningen, Department of Drug Design, A. Deusinglaan 1, 9713 AV Groningen, The Netherlands

*corresponding author: ewa.surmiak@uj.edu.pl; holak@chemia.uj.edu.pl

Abstract

Here, we report a novel class of potent PD-L1/PD-1 inhibitors based on the rigidified biphenyl-inspired structure – terphenyls. Using in-silico docking, we designed and later experimentally shown the efficacy of terphenyl-based scaffolds to inhibit the PD-1/PD-L1 complex formation using various biophysical and biochemical techniques. We also report a high-resolution structure of the PD-L1 complex with our most potent inhibitors allowing the identification of key interactions with PD-L1 at the molecular level. Moreover, we show the efficacy of our most potent inhibitors at activating the antitumor response using primary T-cells derived from healthy donors. This effect was not observed even for the therapeutic antibodies. This makes our compounds prominent candidates for further optimization for anti-PD-L1 cancer treatments.

Introduction

Cancer immunotherapy aims at stimulating immune system's ability to fight cancer as compared to directly killing cancerous cells via more traditional methods such as chemotherapy and radiotherapy (Khalil et al., 2016; Mahoney et al., 2015; Ribas and Wolchok, 2018; Sharma and Allison, 2015, 2020; Shin and Ribas, 2015). Inhibition of negative immune checkpoint regulators is today globally used in clinics and has been acknowledged a Nobel Prize in 2018 in Physiology or Medicine (Ledford et al., 2018). One of the most important immune checkpoints (IC) targeted in cancer immunotherapy is programmed cell death protein 1 (PD-1, known also as CD279) together with its ligand (PD-L1, known also as CD274 or B7-H1) (Dömling and Holak, 2014; Pardoll, 2012; Sharma and Allison, 2015, 2020). The PD-1/PD-L1 axis is responsible for the inhibition of excessive stimulation and normally aims at maintaining the immune tolerance to self-antigens by negatively regulating the immune response (Chen and Flies, 2013; O'Shea and Paul, 2010; Zhou et al., 2009). By blocking the PD-1/PD-L1 interaction, T-cell activation and normalization of antitumor response may be achieved, providing the rationale of this immune checkpoint blockade (ICB) (Hoos, 2016; Sakuishi et

al., 2010). Therefore, the inhibition of the PD-1/PD-L1 complex formation at the cancer cell-T cell interface has become an attractive strategy of cancer immunotherapy (Hoos, 2016).

Traditionally, the inhibition of the PD-1/PD-L1 interaction is achieved via monoclonal antibodies (mAbs) that target either PD-1 (e.g. pembrolizumab, nivolumab, cemiplimab, etc.) or PD-L1 (e.g. atezolizumab, avelumab, durvalumab) (Ribas and Wolchok, 2018) developed using indirect methods such as hybridoma development or phage display (Lee et al., 2019; Nelson et al., 2010). mAbs-based therapies were shown to be more successful than conventional chemotherapy or radiotherapy in terms of overall survival rate and longer progression-free survival groups in various cancers including advanced non–small-cell lung cancer, etc (Borghaei et al., 2015; Hellmann et al., 2018, 2019; Wolchok et al., 2013).

 Despite their medicinal and commercial success, mAbs-bases immunotherapies present numerous shortcomings including a high treatment price, immune-related adverse events (irAEs), and a poor solid tumor penetration (Baldo, 2013; Farid, 2007). Therefore, an alternative, in the form of small molecular and peptide-based inhibitors, was introduced that is believed to overcome those limitations due to small molecules oral bioavailability and lower manufacturing costs while presenting improved pharmacokinetics and diffusion rates (Adams et al., 2015; Huck et al., 2018). Although the PD-1/PD-L1 interface is considered "undruggable" for small-molecule inhibitors (SMI), due to large, flat surface without prominent binding pockets, the number of patents and publications for anti-PD-L1 SMI is constantly increasing, especially after solving the high-resolution structure of the human PD-1/PD-L1 complex as their development process is most often rational design and aided with in-silico docking or modelling routines (Zak et al., 2015, 2016). A common feature of virtually all reported PD-1/PD-L1 SMI is that they are targeted at PD-L1 via biphenyl-based scaffold developed initially by Bristol-Meyers-Squibb (Chupak and Zheng, 2015; Guzik et al., 2019; Lin et al., 2020). The biphenyl moiety was reported to cause dimerization of PD-L1 in high resolution crystals as well as more native environments by nuclear magnetism resonance (NMR) and is speculated to have biological meaning by blocking the export of PD-L1 to ER for correct glycosylation leading to its premature degradation (Chen et al., 2020; Skalniak et al., 2017). As of now, only the compound CA-170 from Curis and Aurigene currently undergoes clinical trials as anti-PD-1/PD-L1 and VISTA SMI. However, CA-170 was shown not to be a direct PD-L1-binder in various biophysical and biochemical assays (Blevins et al., 2019; Musielak et al., 2019).

Here, we report a novel class of potent PD-L1 inhibitors based on the rigidified biphenyl-inspired structure – terphenyls. Using in-silico docking, we designed and later experimentally showed the efficacy of the terphenyl-based scaffold to inhibit the PD-1/PD-L1 complex using various biophysical and biochemical techniques. We also report here a high-resolution structure of the PD-L1 complex with our most potent inhibitors allowing the identification of the key interactions with PD-L1 for their biological activity. Moreover, we have shown the efficacy of our most potent inhibitors to activate the antitumor response using primary T-cells derived from healthy donors.

Results and discussion

Structure optimization based on the homogeneous time-resolved fluorescence (HTRF) assay

Rigidification of a scaffold is a well-known strategy that may result in higher specificity and potency of small-molecule inhibitors (Assadieskandar et al., 2019; Hanson et al., 2007; Lalut et al., 2020; Wu et al., 2018). We have used this approach to modify the biphenyl fragment of anti-PD-L1 inhibitors by removal of the methoxy connector between the biaryl and phenyl rings. The resulting rigidified terphenyl structure was tested in-silico against the parent BMS-1001 compound with AutoDock Vina (Trott and Olson, 2010) integrated into PyRx software (Wolf, 2009).
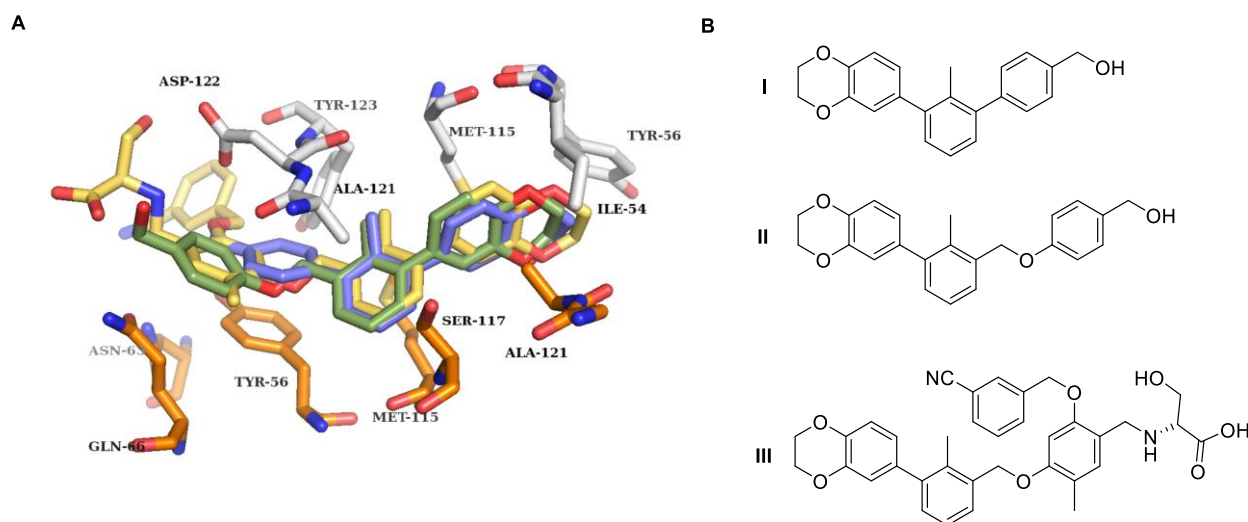
Figure 1. A. Imposition of the modeled complexes of found terphenyl (violet, IB) and corresponding BMS-1001 fragment (green, IIB) and whole BMS-1001 structure (yellow, IIIB) in complex with PD-L1 (grey PDB ID: 5NIU); B. Structures used in molecular modelling: I - terphenyl core fragment; II − corresponding BMS-1001 fragment; III − structure of BMS-1001.

As a result of the molecular docking the (3'-(benzodioxan-6-yl)-2'-methyl-[1,1'-biphenyl]-4-yl)methanol fragment (**I, Figure 1**) emerged that was characterized by the 1.9 kcal/mol stronger binding affinity to the PD-L1 (-12.0 kcal/mol) than the corresponding BMS-1001 fragment (**II, Figure 1**, -10.1 kcal/mol). The affinity of this molecule to PD-L1 was assessed by the homogeneous time-resolved fluorescence (HTRF) assay, giving IC_{50} at 5.49 μM and was confirmed by ^{1}H NMR. NMR showed protein oligomerization after addition of the molecule (**Figure 5A**). Promising preliminary results prompted us to carry out a structural optimization of the found motif. All designed molecules were tested in the HTRF assay to evaluate their activities as the inhibitors of the PD-1/PD-L1 complex (**Table S1**). The results were used for a more rational-based design of the terphenyl extensions to e.g. determine more optimal positions of substituents. In the first step of the process, the impact of the type of the C-2'-attached substituent (R^1), as well as the position of the hydroxymethyl group, for the binding affinity were tested (**Scheme 1, Table 1**).
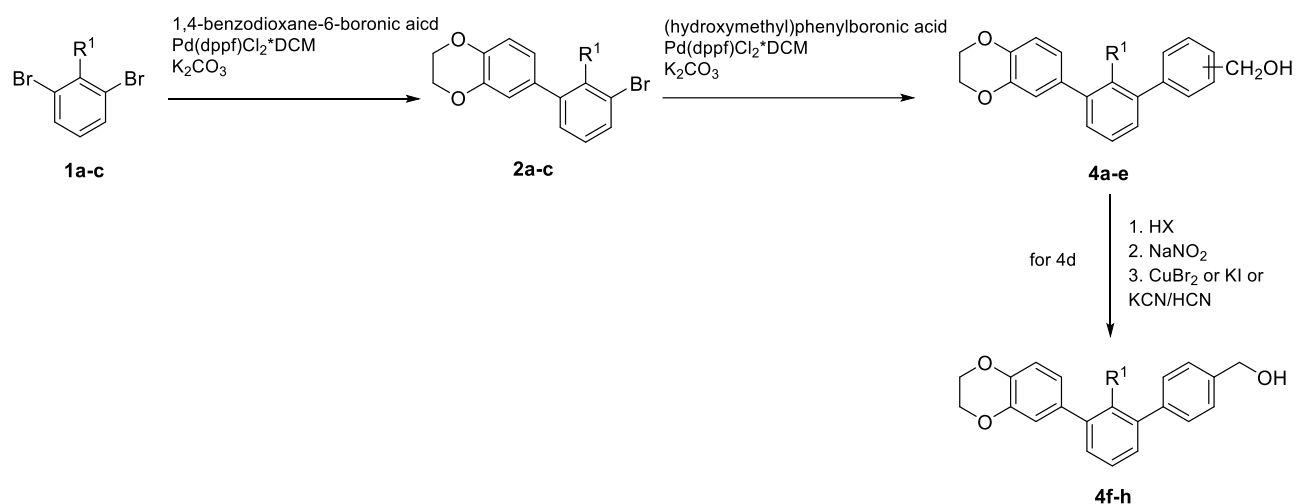
Scheme 1. Synthesis pathway used in R^1 and hydroxymethyl group position optimization. Bromoaryls 1a-c and 2a-c were coupled in Suzuki reaction to terphenyls 4a-e. 4f-h derivatives were obtained in Sandmeyer reaction.

To obtain designed molecules we applied synthetic pathway based mainly on Suzuki cross-coupling reaction. Firstly, appropriate 1,3-dibromoaryls (**1a-c**) were coupled into their 3-benzodioxane derivatives (**2a-c**). Subsequently, biphenlys were taken into second cross-coupling reaction with 2, 3 or 4-(hydroxymethyl)phenylboronic acid leading to the corresponding m-terphenyl derivatives (**4a-e**). C2' nitrile, brominated and iodinated molecules (**4f-h**) were synthesized by Sandmeyer reactions followed by amine-based diazonium salt formation. Results of HTRF assay show clearly, that optimal substituent attached to C2 of middle ring of terphenyl is chlorine with IC_{50} approximately 500 nM (**4e**), however comparable results have been obtained for brominated and cyano derivatives (**4f** and **4h** respectively). Introduction of polar fragment (**4d**) in this region has a negative impact for the molecule affinity to the molecular target. Generally, insertion of the halogen atom in this position is preferred by interaction, but surprisingly, the activity of tested fragments decrease with the growth of the halogen van der Waals radius (**4e-g**).

Table 1. Biological activities of m-terphenyl derivatives obtained in the 1st stage of optimization of R^1 substituent.

Name	R^1	Hydroxymethyl position	XR^2	IC_{50} [μm]
4a	CH_3	para	OH	5.52±0.04
4b	CH_3	meta	OH	++
4c	CH_3	ortho	OH	+
4d	NH_2	para	OH	+++
4e	Cl	para	OH	0.51±0.01

4f	Br	para	OH	0.95±0.02
4g	I	para	OH	+++
4h	CN	para	OH	1.17±0.12

Ranges of the activity of tested compounds in stage I optimization: "very good" (++++) – below 1 µM; "good" (+++) 1-10 µM, "moderate" (++) – 10-50 µM and "bad" (+) – above 50 µM

In parallel, we assessed influence of a further molecule elongation by both the aromatic and aliphatic fragments with different hydrogen bond donor-acceptor properties (**Scheme 2, Table 2**).
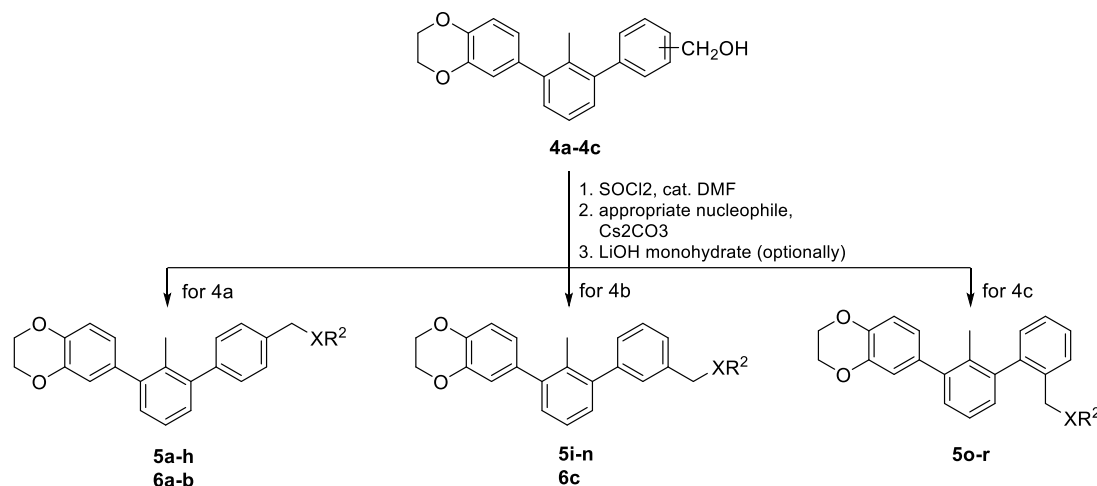
Scheme 2. Synthesis routes leading to elongated m-terphenyl derivatives. Appropriate isomers of 4-(hydroxylethyl)terphenyl were transformed into corresponding chloromethyl derivatives and then used as alkylating agents.

Molecules **5a-s** were obtained in a nucleophilic substitution reaction of the previously prepared benzyl chloride derivatives. The alkyl chlorides were synthesized by transformation of the corresponding 4-hydroxymethylterphenyl derivatives **4a-c** using $SOCl_2$ and catalytic amount of the anhydrous DMF. Then, they were treated with an appropriate nucleophile giving the ethers or tertiary amines (**5a-s, 6a-c**). The double substitution to the amines was prevented by the use of excess of a nucleophile. Furthermore, the bulkiness of the terphenyl fragment additionally precluded double substitution.

Table 2. Biological activities of m-terphenyl derivatives obtained in the 1st stage of optimization of the XR^2 substituent and position in molecule extension

Name	R^1	Hydroxymethyl position	XR^2	IC$_{50}$ [µm]
5b	CH$_3$	para		+

5

5d	CH₃	para		+
5f	CH₃	para		++
5h	CH₃	para		n.a.
6a	CH₃	para		+++
6b	CH₃	para		++++
5j	CH₃	meta		++
5l	CH₃	meta		+
5n	CH₃	meta		++
6c	CH₃	meta		+++
5p	CH₃	ortho		+
5r	CH₃	ortho		n.a

Ranges of the activity of tested compounds in stage I optimization: "very good" (++++) – below 1 μM; "good" (+++) 1-10 μM, "moderate" (++) – 10-50 μM and "bad" (+) – above 50 μM; n.a. - not active

Results obtained from those steps clearly indicated also, that only para elongation, using amine as a building block is beneficial for the interaction (**6b, Table 2**). The attempt of the meta extension of found motif cause a significant drop of activity from IC₅₀ approximately 0.1 μM for **6b** to about 6.0 μM for **6c**. Furthermore, introduction of aromatic fragment in each position also destabilizes the interaction.

In the next stage of the structure optimization, the type of C3-attached ether substituent in the proximal phenyl ring of terphenyl has been considered. In this step we synthesized and assessed in HTRF activities of

a series of different alkoxy derivatives (**Scheme 3, Table 3**), implementing different-length alkyl and cycloalkyl substituents, as well as acetonitrile fragment (**6f-g** and **7a-h**). Initially, we tested piperazine-extended derivatives of assessed ethers (**6f-g**), but observed precipitation during HTRF assay conduction forced us to change the type of used amine to N-(2-aminoethyl)acetamide, increasing significantly solubility in aqueous buffer (**7a-h**).
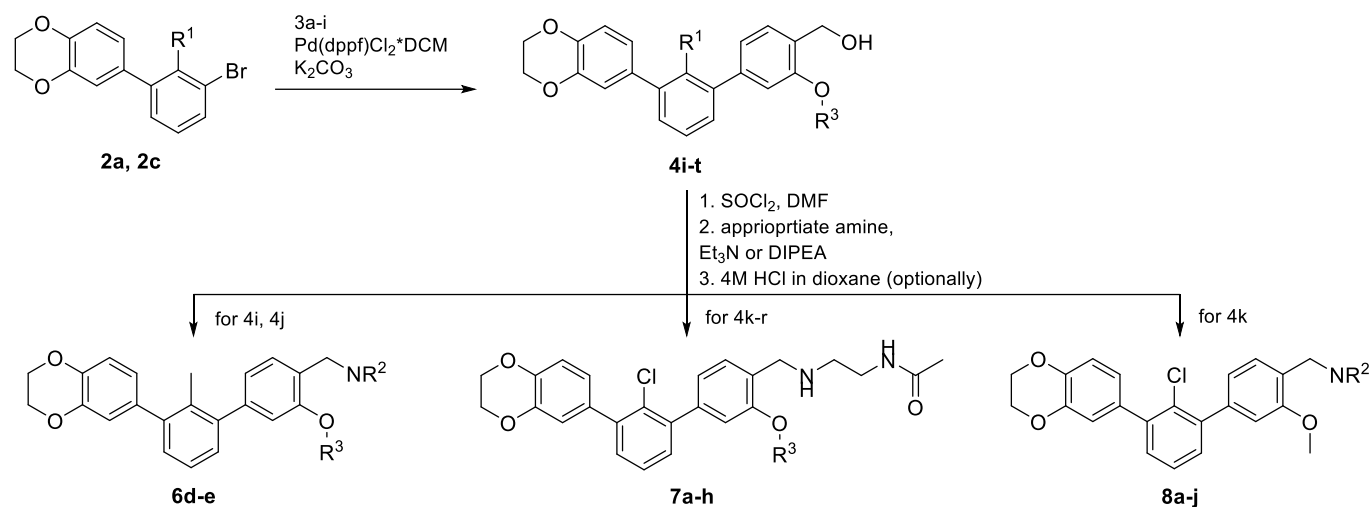
Scheme 3. Synthetic pathway used during R^3 alkoxy fragment and R^2 hydrophilic tail optimization. 3-alkoxyl-4-(hydroxymethyl)terphenyls were transformed into corresponding 4-chloromethyls which were used in the nest step as alkylating agents giving the appropriate amine-extended terphenyls

To get desired molecules, previously used synthesis route has been modified. Firstly, we carried out Williamson alkylation of the 4-bromo-2-hydroxybenzyl alcohol leading to appropriate alkoxy derivative. Then, the intermediates were transformed into corresponding phenylboronic acid pinacol esters (**3a-i**) and coupled with 3-bromobiphenyl derivatives (**2a, 2c**), giving terphenyls. Hydroxymethyl groups of terphenyls were then transformed into corresponding chlorides, which were used as an amine alkylating agents.

Table 3. Biological activities of optimized terphenyls obtained in HTRF assay. Optimization of R^3 alkoxyl substituent.

Name	R^1	XR^2	R^3	IC$_{50}$ [nm]
6d	CH$_3$		CH$_3$	
6e	CH$_3$			+
7a	Cl		CH$_3$	0.82±0.02

Name	R[1]	XR[2]	R[3]	Activity
7b	Cl	—NH–CH₂CH₂–NH–C(=O)CH₃	ethyl (–CH₂CH₃)	+
7c	Cl	—NH–CH₂CH₂–NH–C(=O)CH₃	isobutyl	+++
7d	Cl	—NH–CH₂CH₂–NH–C(=O)CH₃	isopentyl	++
7e	Cl	—NH–CH₂CH₂–NH–C(=O)CH₃	–CH₂CN	+++
7f	Cl	—NH–CH₂CH₂–NH–C(=O)CH₃	–CH₂-cyclobutyl	++
7g	Cl	—NH–CH₂CH₂–NH–C(=O)CH₃	–CH₂-cyclopentyl	+
7h	Cl	—NH–CH₂CH₂–NH–C(=O)CH₃	–CH₂-(3-cyanobiphenyl-3-yl)	+

Ranges of the activity of tested compounds in stage II optimization: "very good" (++++) – below 1 nM; "good" (+++) 1-10 nM, "moderate" (++) – 10-50 nM and "bad" (+) 50 nM – 1µM. Exact values are given for full IC_{50} determination experiments.
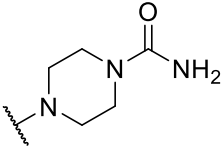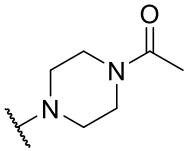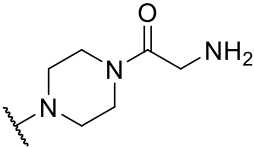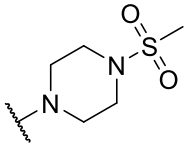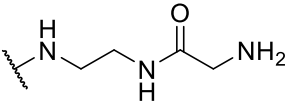
Introduction of methoxy fragment (**7a**) has the greatest impact for the binding to PD-L1 with IC_{50} value at 0.82 nM. Further elongation of etheric part decreases the af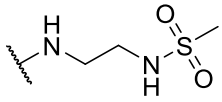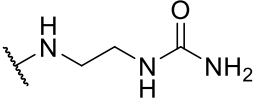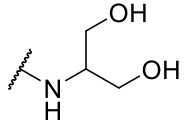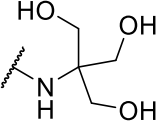finity to the molecular target (**7b-g**). Implementation of the biphenyl motif (**7h**) also cause a drop of inhibitory potency of the molecule. Acetonitrile derivative (**7e**) shows activity comparable with O-methylated **7a** molecule.

The last step of SAR analysis has been focused on hydrophilic tail optimization (**Scheme 3, Table 4**). Maintaining all optimized molecule fragments we synthesized and evaluated biological activities of piperazine (**8a-e**), ethylene diamine (**7a, 8f-h**) and 2-aminoethanol-containing (**8i-j**) terphenyl derivatives.

Table 4. Biological activities of optimized terphenyls obtained in HTRF assay. Optimization of hydrophilic tail NR^2.

Name	R[1]	XR[2]	R[3]	IC_{50} [nm]
8a (PD-134)	Cl	–N(piperazin-1-yl)NH	CH₃	18.09±0.52nM

| Compound		Structure		Activity
8b (PD-142)	Cl	piperazine-N-C(=O)NH₂ (urea)	CH₃	++
8c (PD-145)	Cl	piperazine-N-C(=O)CH₃ (acetyl)	CH₃	+++
8d (MS-34)	Cl	piperazine-N-C(=O)CH₂NH₂	CH₃	Not tested*
8e (PD-144)	Cl	piperazine-N-SO₂CH₃	CH₃	++
8f (PD-151)	Cl	–NH–CH₂CH₂–NH–C(=O)CH₂NH₂	CH₃	++++
8g (PD-141)	Cl	–NH–CH₂CH₂–NH–SO₂CH₃	CH₃	2.07±0.04
8h (PD-153)	Cl	–NH–CH₂CH₂–NH–C(=O)NH₂	CH₃	++++
8i (PD-148)	Cl	–NH–CH(CH₂OH)₂	CH₃	+++
8j (PD-152)	Cl	–NH–C(CH₂OH)₃	CH₃	++++

Ranges of the activity of tested compounds in stage II optimization: "very good" (++++) – below 1 nM; "good" (+++) 1-10 nM, "moderate" (++) – 10-50 nM and "bad" (+) –50 nM – 1μM. Exact values are given for full IC_{50} determination experiments. Compound 8d was not tested due to fluorescence quenching.

The results shown that the type of used solubilizer has a great impact for the affinity to targeted protein. The piperazine derivatives family have been characterized by the lowest potencies in PD-1/PD-L1 complex disruption from tested molecules. The best PD-L1 binder from this group is N-acylated **8c** molecule with IC_{50} approximately 6 nM. The ethylenediamine derivatives (**7a** and **8f-h**) have been characterized by moderate to excellent potencies to inhibition of PD-1/PD-L1 complex formation. Almost all of them shown half maximal inhibitory effect placed in a low nanomolar range. Only sulfonamide-containing molecule (**8g**) has been characterized by IC_{50} value over 2 nM. Introduction of tris(hydroxymethyl)aminomethane (**8j**) maintain

affinity of the molecule to PD-L1 at the level comparable with ethylenediamine derivatives and is characterized by IC_{50} at approximately 0.10 nM. The molecule with attached serinol (**8i**) exhibits moderate activity with approximately 4.7 nM IC_{50} value.

NMR analysis

   Representative molecules from the optimized group were tested for the interaction with PD-L1 using the ^{1}H NMR titration experiment with positive results, and showed on the **Figure 2**. After addition of compounds to hPD-L1 protein we observed broadening of hPD-L1 proton signals in NMR spectra. Binding of **4a**, **7a**, **7e**, and **8j** caused flattening of 1D spectra characteristic for the oligomerization of hPD-L1 observed before with BMS compounds (Guzik et al., 2017). We compered additionally spectra of the interaction of **8j** with hPD-L1 (**Figure 2B**) and mPD-L1 (**Figure 2C**). Only for hPD-L1 changes in proton signals after addition of **8j** to the samples were observed. For mPD-L1 no interactions between mPD-L1 and indicated compound were observed even overtitration of mPD-L1 protein with **8j** (1:10, molar ratio). The results are, therefore, consistent with our previous study were we showed that biphenyl moiety from anti-PD-L1 inhibitors binds to human PD-L1 and not murine analogue (Magiera-Mularz et al., 2021).
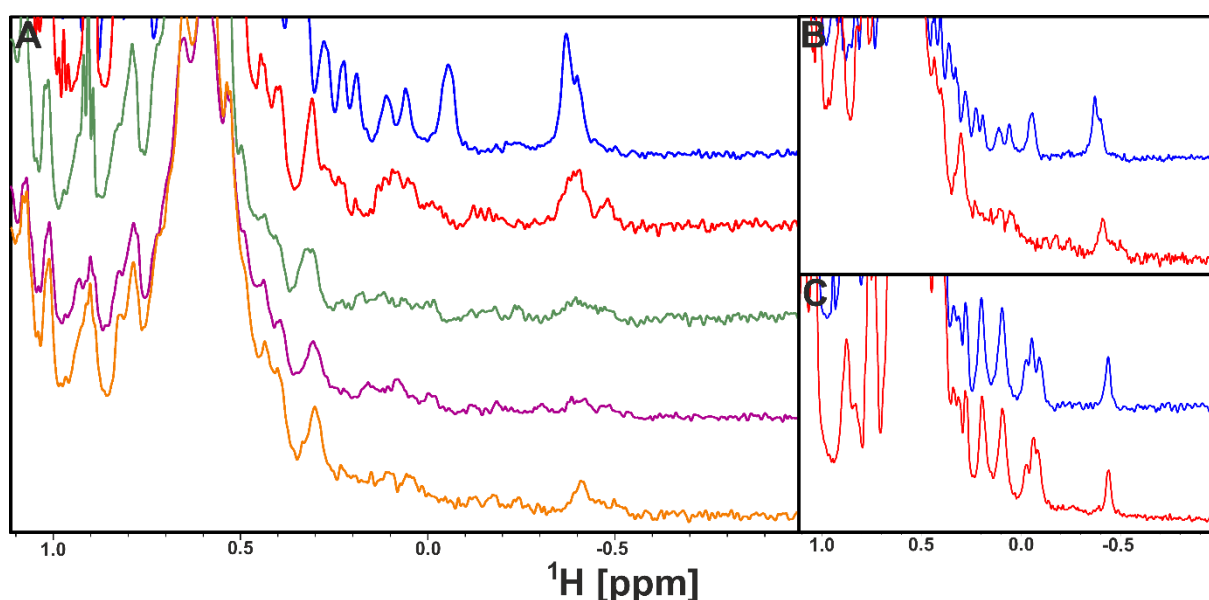
Figure 2. (A) ^{1}H NMR spectra of aliphatic part of human PD-L1 protein (blue) with compound **4a** (red), **7a** (green), **7e** (purple), and **8j** (orange) in the molar ratio 1:1. (B) and (C) the aliphatic region of human PD-L1 and mouse PD-L1 (blue) with **8j** (red) in the molar ratio 1:1 and 1:10, respectively.

In silico ADMET properties

   To illustrate the drug-likeness properties of our compounds selected for *in vitro* evaluation (**7a, 8f-j**), we carried out *in silico* prediction of physicochemical and ADME parameters. The calculations were done using a web-based server SwissADME (Daina et al., 2017). BMS1166 and BMS1001, developed previously by Bristol-Meyers Squibb Company were selected as reference compounds in calculations. As demonstrated in **Table 5**, among all compounds developed by us, five adhere to the Lipinski rule of 5 (Ro5), indicating good drug-likeness properties. Only compound **8h** failed to lay within the permissible range of molecular weight

(MW≤500), although the value for this analogue was near the upper limit of the recommended range. Both BMS1001 and BMS1166 failed to adhere to Lipinski Ro5, because of the higher molecular weight. All of compounds taken for calculations were also predicted to have high gastrointestinal absorption. In contrast, both BMS compounds were flagged with low gastrointestinal absorption. The favorable drug-likeness properties of our compounds (exemplified by **8j**) over BMS1001 and BMS1166 are strictly illustrated on the bioavailability radar maps (**Figure 3**).

Table 5. Physicochemical properties and ADME properties of most active compounds.

Property	Compound								Recommended range
	7a	**8f**	**8g**	**8h**	**8i**	**8j**	**BMS-1166**	**BMS-1001**	
M_w	481	467	482	503	468	456	641	595	<500
H-bond accptors	5	5	6	7	5	6	9	9	<10
H-bond donors	2	2	3	2	3	3	2	3	<5
LogP[a]	4.7	4.3	3.5	3.9	3.7	3.7	4.5	3.6	<5
Violation of Lipinski Ro5	0	0	0	1	0	0	1	1	0
TPSA (Ä²)[b]	68.8	68.8	94.8	94.3	94.9	80.2	121.5	121.45	<140
Rotatable bonds	10	9	10	9	9	8	10	12	<10
PAINS alert	0	0	0	0	0	0	0	0	0
GI[c]	High	High	High	High	High	High	Low	Low	-
BS[d]	0.55	0.55	0.55	0.55	0.55	0.55	0.55	0.55	-

[a]LogP – consensus LogP value calculated as an average of predicted iLogP, XLogP, wLogP, mLogP and Silicos-IT LogP; [b]TPSA – topological polar surface area; [c]GI – gastrointestinal absorption; [d]BS – bioavailability score

Additionally, SwissADME allowed investigating all compounds in terms of containing typical PAINS structural motifs, which may result in false-positive and deceptive activities and, therefore, should be removed from drug discovery campaigns at the early stage (Baell and Holloway, 2010). The analysis suggests, that none of the tested compounds bear any portions that may be responsible for potential artefactual activity. In conclusion, compounds developed by us, due to their favorable pharmacokinetic properties, have good drug-likeness and bioavailability and as such could be considered as good starting points for the further development.
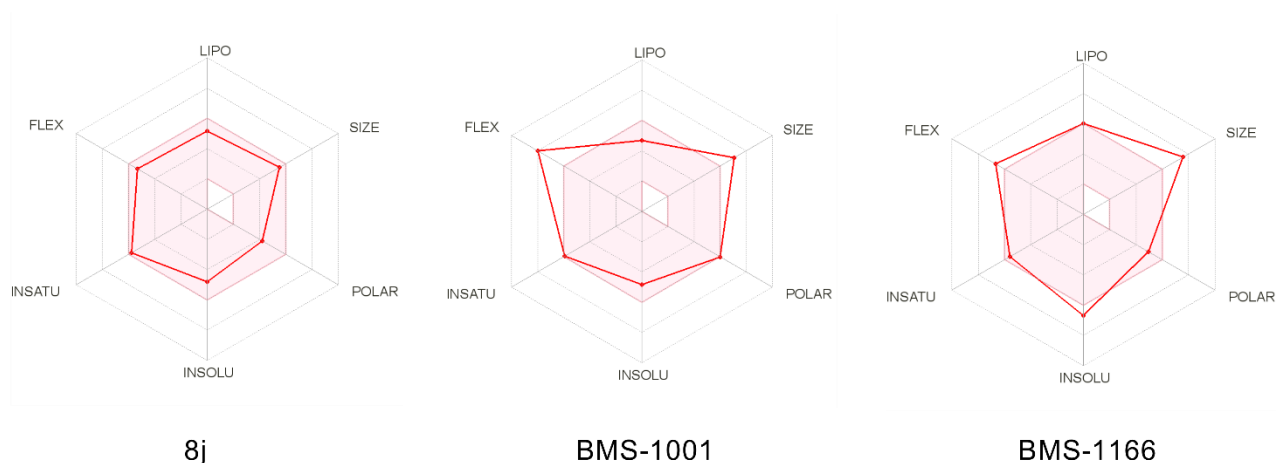
8j	BMS-1001	BMS-1166

Figure 3. The bioavailability radar map for compound **8j**, **BMS-1001** and **BMS-1166**; The pink area represents the optimal range for each property - lipophilicity: XLOGP3 between −0.7 and +5.0, size: M_W between 150 and 500 g/mol, polarity: TPSA between 20 and 130 Å^2, solubility: log S not higher than 6, saturation: fraction of carbons in the sp3 hybridization not less than 0.25, and flexibility: no more than 9 rotatable bonds.

Optimized terphenyl compounds restore T cell activation inhibited by PD-L1

Following a successful optimization of the triphenyl compounds in terms of defining a chlorine as the optimal **R^1** substituent, the methoxy substituent at the meta position (**R^3**) and optimal polar extensions at the para position (**R^2**) of the distal ring of terphenyl, the activity of representative compounds in biological context has been evaluated. To this end, we have first performed a well-recognized and acknowledged PD-1/PD-L1 immune checkpoint blockade (ICB) assay. In the assay, TCR-mediated activation of Jurkat effector cells (Jurkat-ECs) is reduced by the presence of PD-L1, exposed at the surface of CHO/TCRAct/PD-L1 cells (**Figure 4A**). At the addition of PD-1/PD-L1 blockers, full activation of Jurkat-ECs is restored, as presented for a therapeutic anti-PD-L1 antibody, atezolizumab (**Figure 4B**).

Every of the compounds selected for the assay (**7a**, and **8f-8j**) was able to increase the activation of Jurkat-ECs (**Figure 4B**). The best activity, reflected by lowest EC$_{50}$ values (**Figure 4E**), were observed for **8j**, followed by **8h**, **8i**, **7a**, and **8f**. The lowest bioactivity was observed for **8g**. All the compounds were comparable in terms of toxicity towards Jurkat-ECs, with the compounds **7a**, **8f** and **8j** slightly less cytotoxic than **8g**, **8h** and **8i** (**Figure 4C,D**). Importantly, none of the tested compounds was able to increase the activity of Jurkat-ECs at the setups, where PD-L1 was absent. This provides the evidence that the activity of the compounds is PD-L1-dependent and is not related to unspecific activation of T cells. As a result of the highest bioactivity, compounds **8j**, **8h** and **8i** presented the highest selectivity of the desired PD-1/PD-L1-blocking activity versus cytotoxicity (**Figure 4F**). The compounds **8h** and **8j**, which in addition to bioactivity presented IC$_{50}$ vales below 1 nM in HTRF, were directed to further study.
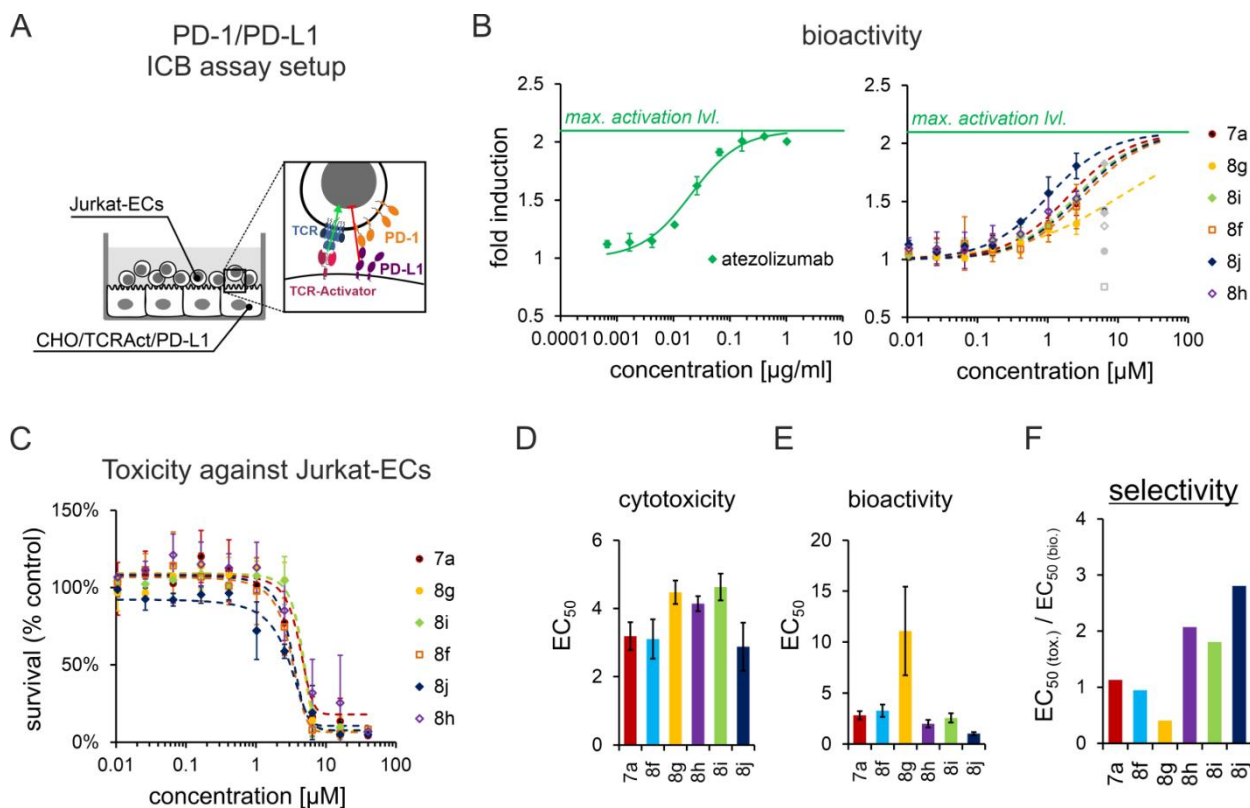
Figure 4. Terphenyl compounds bioactivity and toxicity in Immune Checkpoint Blockade (ICB) assay. (A) A schematic representations of the ICB assay. Jurkat-ECs, Jurkat Effector Cells; TCR, T-Cell Receptor. (B) Dose-response curves of the reactivation of Jurkat-ECs with PD-L1-blocking agents: atezolizumab (left panel) and terphenyl compounds (right panel). Graphs show fold induction of the luminescence signal relative to either untreated (for atezolizumab) or DMSO-treated (for compounds) cells. Data points represent mean ± SD values from 3-5 independent experiments. (C) The long-term (48 hours) cytotoxicity of the tested compounds towards Jurkat-ECs. The graph shows Jurkat-ECs survival relative to DMSO-treated control cells. Data points represent mean ± SD values from 3 independent experiments. (D) Half-maximal effective concentrations (EC_{50}) of the cytotoxicity of the compounds calculated from dose-response curves presented in (C). (E) EC_{50} values of the bioactivity of the compounds in ICB assay, calculated from dose-response curves presented in (B). (F) The selectivity of the bioactivity of the compounds in ICB assay over the cytotoxicity effect towards Jurkat-ECs.

A standard ICB assay relies on artificial Jurkat Effector Cells (Jurkat-ECs), which are surrogates of T cells that allow to monitor TCR-mediated activation by measuring NFAT-dependent expression of Luciferase. In order to verify the potential of the compounds to reactivate PD-L1-blocked primary T cells, a modified assay, termed T-Cell Activation (TCA) was performed (Magiera-Mularz et al., 2020). In the assay, human primary PBMCs are contacted with CHO/TCRAct/PD-L1 cells alone or in the presence of PD-1/PD-L1 blockers, and CD4+ and CD8+ T cells activation is monitored by flow cytometry.

Following the addition of PBMCs to CHO/TCRAct/PD-L1 cells, the activation of both CD4^{+} and CD8^{+} T cells was observed as monitored by the expression of early (CD69), intermediate (CD25 and HLA-DR) and late (PD-1) activation/exhaustion markers (**Figure 5**). This is due to TCR-dependent activation by TCR-Activator ligand presented on CHO/TCRAct/PD-L1 cells. As reported before, the addition of PD-1/PD-L1-blockers in such a setup results in the predominant increase of PD-1 receptor on T cells, but rarely other markers (Magiera-Mularz et al., 2020). In current experiment, this was confirmed for three therapeutic anti-

PD-L1 antibodies, durvalumab, atezolizumab and avelumab (**Figure 5**). Also, for the tested compounds **8h** and **8j**, a significant increase of the numbers of PD-1-positive cells was observed (**Figure 5**). Surprisingly, some decrease of CD69 and CD25 expression was observed for CD4+ cells, which has not been observed before in our studies (**Figure 8**). The addition of the compound **8j**, but neither **8h** nor therapeutic antibodies, increased the numbers of activated, CD25-positive and HLA-DR-positive T cells (**Figure 5**). Altogether, the presented data clearly show biological activity of **8j** in cellular context.
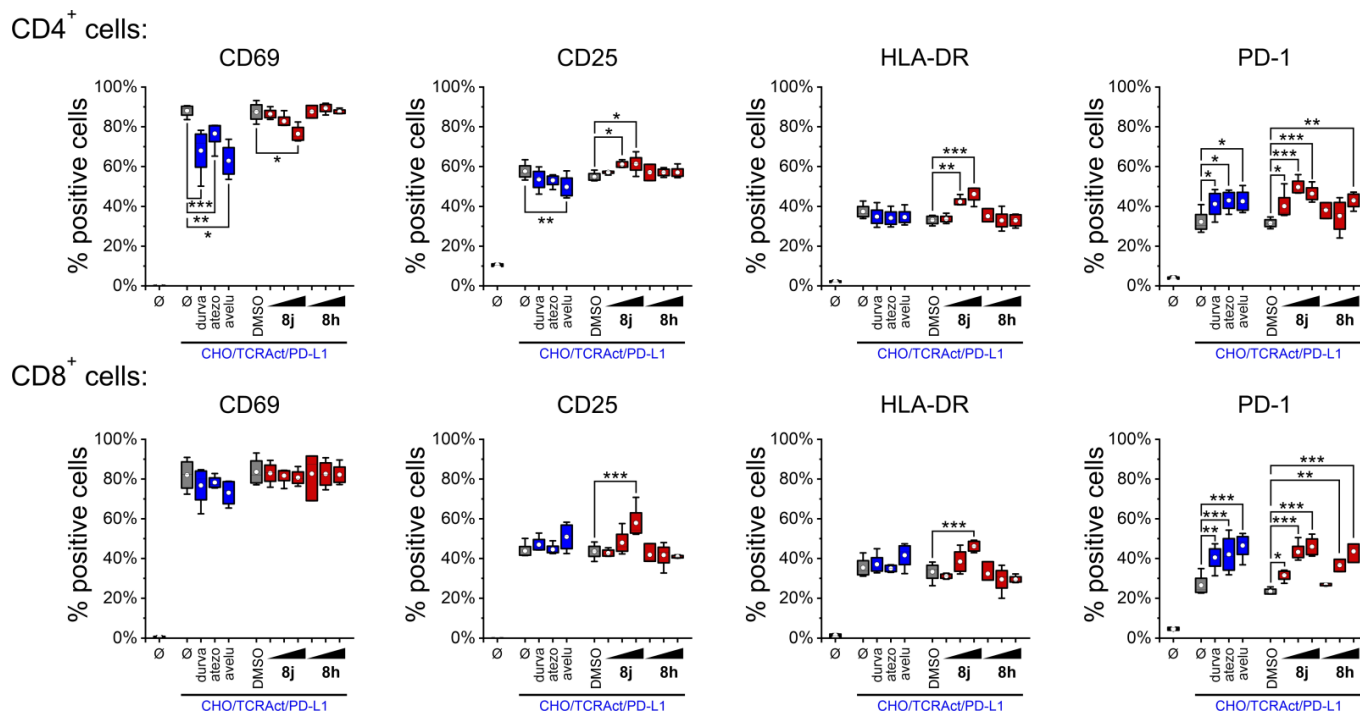

Figure 5. The effect of 8j and 8h on the reactivation of primary T cells pre-blocked by PD-L1-overexpressing cells.

The expression of early (CD69), intermediate (CD25, HLA-DR) and late (PD-1) T cell activation markers was determined by flow cytometry. PBMCs from healthy donors were exposed to CHO cells overexpressing TCR activator and PD-L1 (CHO/TCRAct/PD-L1) for two days. The co-culture was performed in the presence of durvalumab (durva), atezolizumab (atezo), avelumab (avelu) or increasing concentrations of 8j and 8h (concentrations: 0.1 µM, 0.5 µM, or 2.5 µM). ø indicates untreated cells. DMSO-treated cells served as a control for the treatment with compounds. The graphs show fraction of positive cells and represent cumulative data from four donors. Statistical significance was analyzed with one-way ANOVA, followed by Fisher post-hoc test: * $p < 0.05$, ** $p < 0.01$, ***, $p < 0.01$.

Crystal structure

To decipher the molecular basic of the interaction of representative terphenyl compound with the PD-L1 protein, we crystallized and solved the structure of the **8g** compound in complex with target protein at the resolution of 2.2 Å (**Figure 6**). The asymmetric unit of the hPD-L1/**8g** complex contains six protein molecules organized into three dimers with one inhibitor located at the center of interface of each dimer. The electron density map describes each inhibitor molecule allowing position of all moieties in the structure with the fully detailed density for the molecule located at the interface of the dimer. **8g** is mostly buried in the deep and elongated tunnel which is composed of two PD-L1 monomers. The 2,3-dihydro-1,4-benzodioxinyl group creates standard interaction with $_A$Tyr56 previously observed by us for the BMS-202, BMS- 1001 and BMS-

1166 compounds (Guzik et al., 2017; Skalniak et al., 2017). The central terphenyl moiety is stabilized by plenty of hydrophobic contacts with: $_B$Tyr56, $_A$Met115, $_B$Met115, $_A$Ala121, $_B$Ala121. The chlorine substituent attached to this moiety forms additional halogen bond with the backbone carbonyl of $_A$Asp122 providing rationale for the enhanced inhibitory effect of haloganated inhibitors at R^1 position. The methoxy substituent at the meta position of the distal ring of terphenyl is also additionally stabilized by hydrophobic interaction with: $_B$Ile54, $_B$Val68 pointing out the importance of this substituent. At the other side of the tunnel, the sulfonoamide polar extension forms hydrogen bond with the carbonyl of $_A$Asp122 sidechain and is largely water-exposed.
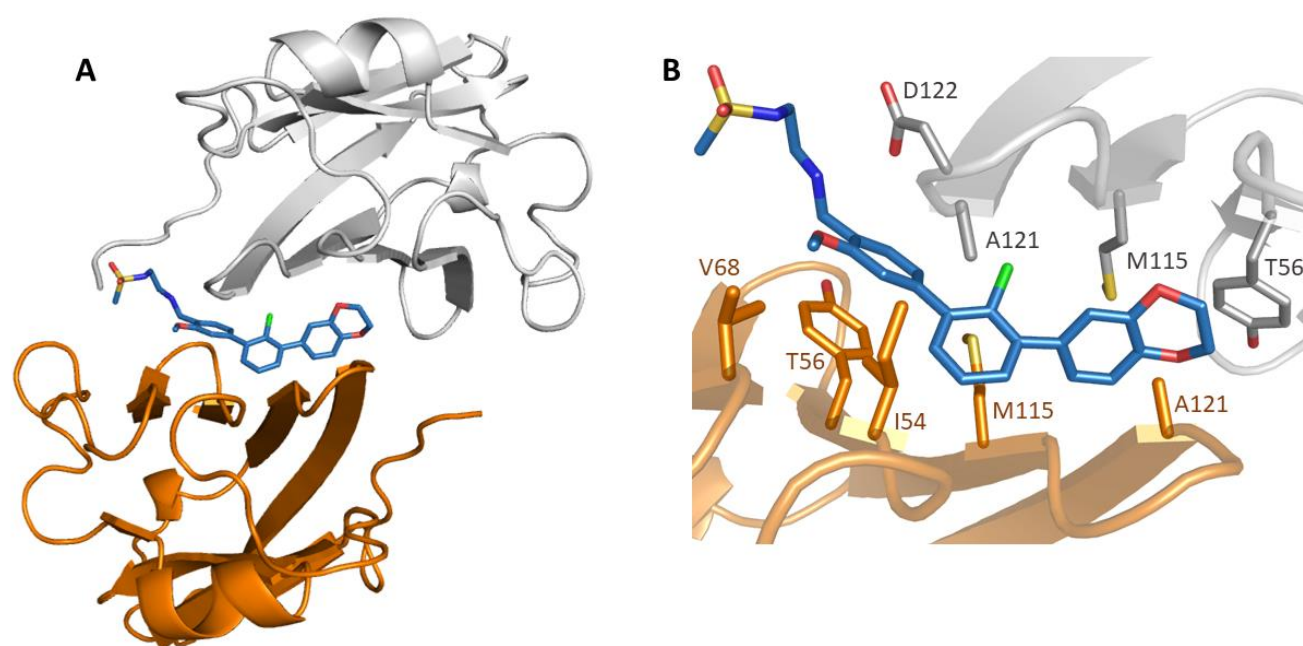
Figure 6. Cocrystal X-ray structure of **8g** bound to Ig-like V-type domain of human PD-L1. (A) Arrangement of the molecules in the crystal structure – two PD-L1 molecules (gray and orange) form a single pocket accommodating **8g** compound (blues). (B) Detailed interactions of **8g** at the binging cleft of PD-L1. Inhibitor binds at a hydrophobic cavity formed upon the PD-L1 dimerization. Colour coding as in (A)

Conclusions

Herein, we demonstrate a novel group of anti-PD-L1 small molecular inhibitors based on the concept of the rigidification of the biphenyl moiety by the addition of another phenyl ring. Such terphenyl based scaffolds exhibit high inhibitory activity against PD-1/PD-L1 complex formation both in a common biophysical assay, such as HTRF as well as cell based assays. Our best compounds activated Jurkat-ECs to levels comparable to those of control antibody, despite being considerably smaller. Similarly to other reported in the literature anti-PD-L1 inhibitors, our compounds dimerized human PD-L1 as presented by NMR and X-ray crystallography studies, however they do not possess the cross-reactivity to murine PD-L1 analog. Our best compound adhere to Lipinski's rule of five, which is a golden standard for drug discovery process, including their molecular

size, unlike many other reported in the literature anti-PD-L1 small molecular inhibitors such as BMS-1166. Moreover, they are all characterized by relatively low cytotoxicity above 3 µM and high gastrointestinal absorption coefficient as estimated using SwissADME server suggesting a possible oral administration of our compounds, which would be advantageous compared to intravenous administration of monoclonal antibodies. Our most potent compound, **8j**, is characterized by exceptionally low IC_{50} estimated below 10 pM as well as proven potency in cell-based assay with EC_{50} of ca. 1 uM. Most importantly, the addition of the compound **8j** to the co-culture of PBMCs and CHO/TCRAct/PD-L1 cells not only induced PD-1 expression, but also increased the numbers of CD25-positive and HLA-DR-positive T cells, which was not observed even for therapeutic antibodies. This shows the potency of the compound towards primary human T cells and designates **8j** a very prominent candidate for further optimization for anti-PD-L1 cancer treatments.

Materials and methods

Synthesis

All syntheses were performed using general procedures summarized in **Schemes 2-4** and as described in Supporting Information. Reagents were obtained from commercial suppliers (Sigma Aldrich, ABCR, Acros Organics, Appollo Scientific, AK Scientific) and used without further purification unless otherwise noted. Anhydrous solvents were purchase from Sigma-Aldrich or Alfa-Aesar, anhydrous Et_2O and THF were distilled from sodium-benzophenone and stored over molecular sieves (4Å, 3-5 mm beads). Nuclear magnetic resonance spectra were recorded on a Bruker Avance 600 spectrometer {^1H NMR (600 MHz), ^{13}C NMR (151 MHz)}. Chemical shifts for ^1H NMR were reported as d values and coupling constants were in hertz (Hz). The following abbreviations were used for spin multiplicity: s = singlet, s_{broad} = broad singlet, d = doublet, t = triplet, q = quartet, quin = quintet, dd = double of doublets, ddd = double doublet of doublets, m = multiplet. Chemical shifts for ^{13}C NMR were reported in d relative to the solvent peak. Thin layer chromatography was performed on SigmaAldrich/Fluka precoated silica gel plates (0.20 mm thick, particle size 25 mm). Flash chromatography was performed on a Reveleris® X2 Flash Chromatography, using Grace® Reveleris Silica flash cartridges. The LC-MS measurements were performed on the UPLC-MS/MS system consisted of a Waters ACQUITY® UPLC® (Waters Corporation, Milford, MA, USA) coupled to a Waters TQD mass spectrometer (electrospray ionization mode ESI-tandem quadrupole). Chromatographic separations were carried out using the Acquity UPLC BEH (bridged ethyl hybrid) C_{18} column; 2.1 × 100 mm, and 1.7 µm particle size, equipped with Acquity UPLC BEH C18 VanGuard pre-column; 2.1 × 5 mm, and 1.7 µm particle size. The column was maintained at 40°C, and eluted under gradient conditions using from 95% to 0% of eluent A over 10 min, at a flow rate of 0.3 mL min^{-1}. Eluent A: water/formic acid (0.1%, v/v); eluent B: acetonitrile/formic acid (0.1%, v/v). The purity of all final compounds determined using chromatographic LC-MS was >95%. HRMS were carried out by the Laboratory for Forensic Chemistry Faculty of Chemistry, Jagiellonian University with the microOTOF-QII (Bruker) spectrometer using ESI ionization technique.

Protein expression and purification

E. coli strain BL21 was transformed with pET-21b plasmid carrying PD-L1 gene (amino acids 18-134). The bacteria were cultured in LB at 37°C until OD_{600}nm of 0,6 when the recombinant protein production was induced with 1 mM IPTG. The protein production was continued overnight. Inclusion bodies were collected by centrifugation, washed twice with 50 mM Tris-HCl pH 8.0 containing 200 mM NaCl, 10 mM EDTA, 10 mM 2-mercaptoethanol and 0.5% Triton X-100, followed by a single wash with the same buffer but with no Triton X-100. The washed inclusion bodies were resuspended overnight in 50 mM Tris-HCl pH 8.0, 6 M GuHCl, 200 mM NaCl and 10 mM 2-mercaptoethanol and clarified with centrifugation. Refolding of PD-L1 was performed by drop-wise dilution into 0.1 M Tris-HCl pH 8.0 containing 1 M L-arginine hydrochloride, 0.25 mM oxidized glutathione and 0.25 mM reduced glutathione. The refolded protein was dialyzed 3 times against 10 mM Tris-HCl pH 8.0 containing 20 mM NaCl and purified by size exclusion chromatography using Superdex 75 and dialysis buffer. The quality of the refolded protein was evaluated by SDS-PAGE and NMR.

Homogenous Time Resolved Fluorescence

HTRF was performer using the certified Cis-Bio assay according to the manufacturer's guidelines. The experiments were performed at 5 nM of h-L1 and 50 nM of hPD-1 in the final formulation at 20 μL final volume in the well. To determine the half maximal inhibitory concentration (IC_{50}) of tested compounds, measurements were performed on two individual dilution series, unless states otherwise. After mixing all components according to Cis-Bio protocol, the plate was left for 2h incubation at room temperature followed by TR-FRET measurement on Tecan Spark 20M. Collected data was background subtracted on the negative control, normalized on the positive control, averaged and fitted with normalized Hill's equation to determine the IC_{50} value using *Mathematica 12*. For some compounds, there was insufficient datapoints to determine the IC_{50} as they were measured in scouting mode. The inhibitory constants for those compounds were approximated by translation of the Hill's fit of fully described compound to match the experimental datapoints. Since all compounds reported here are closely related, the slope of Hill's fit that determines the shape of the curve is therefore similar across them. Nevertheless, the IC_{50}s of such compound is reported in bins of "very good" (++++), "good" (+++), "moderate" (+) and "bad" (+) and the legend is reported underneath each table.

PD-L1 cocrystallization

Purified PD-L1 in 10 mM Tris-HCl pH 8.0, 20 mM NaCl buffer was concentrated to 5 mg/ml, mixed with the **8g** inhibitor in 1:3 molar ratio (protein:compound) and clarified. Supernatant was used for screening using commercially available buffer sets. Diffraction-quality crystals were obtained at room temperature from the condition containing: 0.1 M sodium cocodylate pH 6.5, 25 % PEG 4000. The crystal was flash-cooled in liquid nitrogen.

Crystal structure determination and refinement

The X-ray diffraction data were collected at the BL14.1 beamline operated by the Helmholtz-Zentrum Berlin (HZB) at the BESSY II (Berlin Adlershof, Germany) (Mueller et al., 2012). The data were indexed,

integrated, and scaled using XDS, XSCALE, and Aimless (Evans and Murshudov, 2013; Kabsch, 2010; Krug et al., 2012). Initial phases were obtained by molecular replacement calculated in Phaser (McCoy et al., 2007). The model building was performed in Coot and refinement was performed using Phenix or PDB-REDO server (Adams et al., 2010; Emsley and Cowtan, 2004; Joosten et al., 2014). Water molecules were added automatically and inspected manually.

Cell culture

CHO-K1 cells, CHO-K1 cells overexpressing TCR activator (CHO/TCRAct), PD-L1-expressing CHO/TCRAct cells (CHO/TCRAct/PD-L1), and Jurkat-ECs T cells overexpressing PD-1 and carrying a luciferase reporter gene under the control of Nuclear Factor of Activated T-cells Response Element (NFAT-RE) were obtained from Promega and cultured in RPMI-1640 medium (Biowest) supplemented with 10% Fetal Bovine Serum (FBS, Biowest) and 200 mM L- Glutamine (Biowest). G418 (250 µg/ml, InvivoGen) and Hygromycin B Gold (50 µg/ml, InvivoGen) were also added to the culture medium as selection antibiotics. The overexpression of PD-L1 and TCR ligand in CHO/TCRAct/PD-L1 cells, and overexpression of PD-1 in Jurkat-ECs were confirmed by flow cytometry and western blot analysis. PCR tests for *Mycoplasma sp.* contamination (Van Kuppeveld et al., 1992) were routinely performed and indicated negative results for both cell lines.

Cytotoxicity assay

The cytotoxicity of compounds was verified towards Jurkat-ECs, since these cells provide the readout in the ICB assay and present much higher degree of susceptibility to the compounds' toxicity than CHO-K1 cells (not shown). Jurkat-ECs were seeded on 96-well transparent plates in the presence of increasing concentrations of the compounds with DMSO-treated cells as a control. The concentration of DMSO was kept constant (0.1%). After 48 h of incubation, a tetrazolizum reagent, Biolog Redox Dye MIX MB (Biolog), was added according to the manufacturer's protocol, and culture plates were incubated for additional 2 h (37°C, 5% CO2). The absorbance was measured using Spark microplate reader (Tecan) at 590 nm with 750 nm as a reference. Half-maximal effective concentrations (EC50 values) were calculated from the dose-response curve using OriginPro (OriginLab) software.

PD-1/PD-L1 immune checkpoint blockade assay

The functional assay of the blockade of PD-1/PD-L1 interaction in vitro (PD-1/PD-L1 Blockade Bioassay, Promega) was performed according to the manufacturer's protocol. CHO/TCRAct/PD-L1 cells or CHO/TCRAct or CHO-K1 cells were seeded on 96-well white plates at the density of 10 000 cells/well and the next day overlaid with Jurkat T cells (20 000 cells/well) in the presence of increasing concentrations of the compounds with DMSO-only as a control (the concentration of DMSO was kept constant at 0.1%) or atezolizumab, as a positive control, anti-PD-L1 monoclonal antibody (Selleckchem). The 2.5-fold dilutions of atezolizumab were prepared in the assay buffer (RPMI 1640+1%FBS) on the day of the assay. Activation of

the Jurkat T cells, reflected by luciferase activity, was monitored by luminescence measurements after 6 h of incubation (37°C, 5%CO2), and 20 min additional incubation with the Bio-Glo™ Assay reagent (Promega) in a room temperature. The luminescence was read on the Spark microplate reader (Tecan). Half-maximal effective concentrations (EC50 values) were calculated from the Hill curve fitting to the experimental data using Origin Pro 2020 software (OriginLab).

The isolation of PBMC

ACDA-treated blood from healthy donors was purchased from the Regional Center of Blood Donation and Blood Therapy in Krakow, Poland. Peripheral Blood Mononuclear Cells (PBMC) were isolated from the whole blood by a density gradient centrifugation using Pancoll human separating solution (PAN-Biotech GmbH, Aidenbach, Germany). Separated cells were washed and resuspended in RPMI 1640 medium (Biowest), containing 10% fetal bovine serum (FBS, Biowest).

T-Cell Activation (TCA) assay

PBMCs were added at the amount of 3×10^5 to CHO, CHO/TCRAct, or CHO/TCRAct/PD-L1 cells pre-seeded on 24-well plates in the presence of either anti PD-L1 monoclonal antibodies (at the final concentration 5µg/ml): durvalumab (Selleckchem), atezolizumab (Selleckchem) or avelumab (MedChemExpress), or tested compounds at the concentrations 0.1, 0.5, and 2.5 µM. Untreated cells were used as controls for antibody treatment, awhile DMSO-treated cells (0.1% (v/v)) were used as controls for compounds treatment. The cells were incubated for 48 h (37°C, 5% CO2) and then detached from the plates with TrypLe Select Enzyme (Thermo Fisher). PBMCs were stained for 20 minutes at room temperature with the antibodies: anti-CD4-FITC, anti-CD8-BV510, anti-CD69-APC, anti-CD25-PE, anti-HLA-DR-PerCP, anti-PD1-PECy7 (Becton Dickinson Biosciences, BD). Following two washing steps, the cells were analyzed with FACSCanto II cytometer. Data analysis was carried out with FlowJo software, followed by statistical significance calculations done with Origin Pro 2020 software (OriginLab).

NMR analysis

NMR spectra were recorded in PBS pH 7.4 containing 10% (v/v) of D2O added to the samples to provide the lock signal. Water suppression was carried out using the WATERGATE sequence. All the spectra were recorded at 300 K using a Bruker Avance 600 MHz spectrometer with the Cryo-Platform. The spectra were recorded at the ligand/protein ratio 1:1. The sample were prepared by adding small amounts of a 50 mM ligand stock solution in DMSO to the protein solution (0.20 ml) of PD-L1 fragment at a concentration of 0.2 mM. Spectra were visualized using TopSpin 4.0.2.

In silico **ADMET evaluation**

All parameters were predicted using a free web-based tool SwissADME. Compound 2D structures were generated in the molecular sketcher and transferred to the input list as SMILES. All results, including

physicochemical properties, lipophilicity, water solubility, pharmacokinetics, drug-likeness and medicinal chemistry properties were collected and exported as the .csv file.

Acknowledgments

References

Adams, J.L., Smothers, J., Srinivasan, R., and Hoos, A. (2015). Big opportunities for small molecules in immuno-oncology. Nat. Rev. Drug Discov. *14*, 603–622.

Adams, P.D., Afonine, P. V., Bunkóczi, G., Chen, V.B., Davis, I.W., Echols, N., Headd, J.J., Hung, L.W., Kapral, G.J., Grosse-Kunstleve, R.W., et al. (2010). PHENIX: A comprehensive Python-based system for macromolecular structure solution. Acta Crystallogr. Sect. D Biol. Crystallogr. *66*, 213–221.

Assadieskandar, A., Yu, C., Maisonneuve, P., Kurinov, I., Sicheri, F., and Zhang, C. (2019). Rigidification Dramatically Improves Inhibitor Selectivity for RAF Kinases. ACS Med. Chem. Lett.

Baell, J.B., and Holloway, G.A. (2010). New Substructure Filters for Removal of Pan Assay Interference Compounds (PAINS) from Screening Libraries and for Their Exclusion in Bioassays. J. Med. Chem. *53*, 2719–2740.

Baldo, B. (2013). Adverse events to monoclonal antibodies used for cancer therapy: Focus on hypersensitivity responses. Oncoimmunology *2*, e26333.

Blevins, D.J., Hanley, R., Bolduc, T., Powell, D.A., Gignac, M., Walker, K., Carr, M.D., Hof, F., and Wulff, J.E. (2019). *In Vitro* Assessment of Putative PD-1/PD-L1 Inhibitors: Suggestions of an Alternative Mode of Action. ACS Med. Chem. Lett.

Borghaei, H., Paz-Ares, L., Horn, L., Spigel, D.R., Steins, M., Ready, N.E., Chow, L.Q., Vokes, E.E., Felip, E., Holgado, E., et al. (2015). Nivolumab versus Docetaxel in Advanced Nonsquamous Non-Small-Cell Lung Cancer. N. Engl. J. Med.

Chen, L., and Flies, D.B. (2013). Molecular mechanisms of T cell co-stimulation and co-inhibition. Nat. Rev. Immunol. *13*, 227–242.

Chen, F.F., Li, Z., Ma, D., and Yu, Q. (2020). Small-molecule PD-L1 inhibitor BMS1166 abrogates the function of

PD-L1 by blocking its ER export. Oncoimmunology *9*, e1931153.

Chupak, L.S., and Zheng, X. (2015). Compounds useful as immunomodulators, Bristol-Myers Squibb Company, WO 2015/034820 A1.

Daina, A., Michielin, O., and Zoete, V. (2017). SwissADME: a free web tool to evaluate pharmacokinetics, drug-likeness and medicinal chemistry friendliness of small molecules. Sci. Rep. *7*, 42717.

Dömling, A., and Holak, T.A. (2014). Programmed Death-1: Therapeutic Success after More than 100 Years of Cancer Immunotherapy. Angew. Chemie Int. Ed. *53*, 2286–2288.

Emsley, P., and Cowtan, K. (2004). Coot: Model-building tools for molecular graphics. Acta Crystallogr. Sect. D Biol. Crystallogr. *60*, 2126–2132.

Evans, P.R., and Murshudov, G.N. (2013). How good are my data and what is the resolution? Acta Crystallogr. Sect. D Biol. Crystallogr. *69*, 1204–1214.

Farid, S.S. (2007). Process economics of industrial monoclonal antibody manufacture. J. Chromatogr. B *848*, 8–18.

Guzik, K., Zak, K.M., Grudnik, P., Magiera, K., Musielak, B., Törner, R., Skalniak, L., Dömling, A., Dubin, G., and Holak, T.A. (2017). Small-Molecule Inhibitors of the Programmed Cell Death-1/Programmed Death-Ligand 1 (PD-1/PD-L1) Interaction via Transiently Induced Protein States and Dimerization of PD-L1. J. Med. Chem. *60*, 5857–5867.

Guzik, K., Tomala, M., Muszak, D., Konieczny, M., Hec, A., Błaszkiewicz, U., Pustuła, M., Butera, R., Dömling, A., and Holak, T.A. (2019). Development of the inhibitors that target the PD-1/PD-L1 interaction—a brief look at progress on small molecules, peptides and macrocycles. Molecules *24*, 1–32.

Hanson, W.M., Domek, G.J., Horvath, M.P., and Goldenberg, D.P. (2007). Rigidification of a Flexible Protease Inhibitor Variant upon Binding to Trypsin. J. Mol. Biol. *366*, 230–243.

Hellmann, M.D., Ciuleanu, T.-E., Pluzanski, A., Lee, J.S., Otterson, G.A., Audigier-Valette, C., Minenza, E., Linardou, H., Burgers, S., Salman, P., et al. (2018). Nivolumab plus Ipilimumab in Lung Cancer with a High Tumor Mutational Burden. N. Engl. J. Med. *378*, 2093–2104.

Hellmann, M.D., Paz-Ares, L., Bernabe Caro, R., Zurawski, B., Kim, S.-W., Carcereny Costa, E., Park, K., Alexandru, A., Lupinacci, L., de la Mora Jimenez, E., et al. (2019). Nivolumab plus Ipilimumab in Advanced Non–Small-Cell Lung Cancer. N. Engl. J. Med. *381*, 2020–2031.

Hoos, A. (2016). Development of immuno-oncology drugs-from CTLA4 to PD1 to the next generations. Nat. Rev. Drug Discov. *15*, 235–247.

Huck, B.R., Kötzner, L., and Urbahns, K. (2018). Small Molecules Drive Big Improvements in Immuno-Oncology Therapies. Angew. Chemie Int. Ed. *57*, 4412–4428.

Joosten, R.P., Long, F., Murshudov, G.N., and Perrakis, A. (2014). The PDB-REDO server for macromolecular structure model optimization. IUCrJ *1*, 213–220.

Kabsch, W. (2010). Xds. Acta Crystallogr. D. Biol. Crystallogr. *66*, 125–132.

Khalil, D.N., Smith, E., Brentjens, R., and Wolchok, J.D. (2016). The future of cancer treatment: immunomodulation, CARs and combination immunotherapy. Nat. Rev. Clin. Oncol. *13*, 273–290.

Krug, M., Weiss, M.S., Heinemann, U., and Mueller, U. (2012). {\it XDSAPP}: a graphical user interface for the convenient processing of diffraction data using {\it XDS}. J. Appl. Crystallogr. *45*, 568–572.

Van Kuppeveld, F.J.M., Van der Logt, J.T.M., Angulo, A.F., Van Zoest, M.J., Quint, W.G.V., Niesters, H.G.M., Galama, J.M.D., and Melchers, W.J.G. (1992). Genus- and species-specific identification of mycoplasmas by 16S rRNA amplification. Appl. Environ. Microbiol. *58*, 2606–2615.

Lalut, J., Payan, H., Davis, A., Lecoutey, C., Legay, R., Sopkova-de Oliveira Santos, J., Claeysen, S., Dallemagne, P., and Rochais, C. (2020). Rational design of novel benzisoxazole derivatives with acetylcholinesterase inhibitory and serotoninergic 5-HT4 receptors activities for the treatment of Alzheimer's disease. Sci. Rep.

Ledford, H., Else, H., and Warren, M. (2018). Cancer immunologists scoop medicine Nobel prize. Nature *562*, 20–21.

Lee, H.T., Lee, S.H., and Heo, Y.S. (2019). Molecular interactions of antibody drugs targeting PD-1, PD-L1, and CTLA-4 in immuno-oncology. Molecules.

Lin, X., Lu, X., Luo, G., and Xiang, H. (2020). Progress in PD-1/PD-L1 pathway inhibitors: From biomacromolecules to small molecules. Eur. J. Med. Chem. *186*, 111876.

Magiera-Mularz, K., Kocik, J., Musielak, B., Plewka, J., Sala, D., Machula, M., Grudnik, P., Hajduk, M., Czepiel, M., Siedlar, M., et al. (2021). Human and mouse PD-L1: similar molecular structure, but different druggability profiles. iScience *24*, 101960.

Magiera-Mularz, K., Kuska, K., Skalniak, L., Grudnik, P., Musielak, B., Plewka, J., Kocik, J., Stec, M., Weglarczyk, K., Sala, D., et al. (2020). Macrocyclic Peptide Inhibitor of PD-1/PD-L1 Immune Checkpoint. Adv. Ther. 2000195.

Mahoney, K.M., Rennert, P.D., and Freeman, G.J. (2015). Combination cancer immunotherapy and new immunomodulatory targets. Nat. Rev. Drug Discov. *14*, 561–584.

McCoy, A.J., Grosse-Kunstleve, R.W., Adams, P.D., Winn, M.D., Storoni, L.C., and Read, R.J. (2007). Phaser crystallographic software. J. Appl. Crystallogr. *40*, 658–674.

Mueller, U., Darowski, N., Fuchs, M.R., Förster, R., Hellmig, M., Paithankar, K.S., Pühringer, S., Steffien, M., Zocher, G., and Weiss, M.S. (2012). Facilities for macromolecular crystallography at the Helmholtz-Zentrum Berlin. J. Synchrotron Radiat. *19*, 442–449.

Musielak, B., Kocik, J., Skalniak, L., Magiera-Mularz, K., Sala, D., Czub, M., Stec, M., Siedlar, M., Holak, T.A., and Plewka, J. (2019). CA-170 - A Potent Small-Molecule PD-L1 Inhibitor or Not? Molecules *24*, 2804.

Nelson, A.L., Dhimolea, E., and Reichert, J.M. (2010). Development trends for human monoclonal antibody therapeutics. Nat. Rev. Drug Discov. *9*, 767–774.

O'Shea, J.J., and Paul, W.E. (2010). Mechanisms underlying lineage commitment and plasticity of helper CD4+T cells. Science *327*, 1098–1102.

Pardoll, D.M. (2012). The blockade of immune checkpoints in cancer immunotherapy. Nat. Rev. Cancer *12*, 252–264.

Ribas, A., and Wolchok, J.D. (2018). Cancer immunotherapy using checkpoint blockade. Science (80-.). *359*, 1350–1355.

Sakuishi, K., Apetoh, L., Sullivan, J.M., Blazar, B.R., Kuchroo, V.K., and Anderson, A.C. (2010). Targeting Tim-3 and PD-1 pathways to reverse T cell exhaustion and restore anti-tumor immunity. J. Exp. Med. *207*, 2187–2194.

Sharma, P., and Allison, J.P. (2015). The future of immune checkpoint therapy. Science (80-.). *348*, 56–61.

Sharma, P., and Allison, J.P. (2020). Dissecting the mechanisms of immune checkpoint therapy. Nat. Rev. Immunol. *20*, 75–76.

Shin, D.S., and Ribas, A. (2015). The evolution of checkpoint blockade as a cancer therapy: What's here, what's next? Curr. Opin. Immunol. *33*, 23–35.

Skalniak, L., Zak, K.M., Guzik, K., Magiera, K., Musielak, B., Pachota, M., Szelazek, B., Kocik, J., Grudnik, P., Tomala, M., et al. (2017). Small-molecule inhibitors of PD-1/PD-L1 immune checkpoint alleviate the PD-L1-induced exhaustion of T-cells. Oncotarget *8*, 72167–72181.

Trott, O., and Olson, A.J. (2010). AutoDock Vina: Improving the speed and accuracy of docking with a new scoring function, efficient optimization, and multithreading. J. Comput. Chem. *31*, 455–461.

Wolchok, J.D., Kluger, H., Callahan, M.K., Postow, M.A., Rizvi, N.A., Lesokhin, A.M., Segal, N.H., Ariyan, C.E., Gordon, R.A., Reed, K., et al. (2013). Nivolumab plus Ipilimumab in advanced melanoma. N. Engl. J. Med. *369*, 122–133.

Wolf, L.K. (2009). PyRx. C&EN *87*.

Wu, L., Qian, D.-Q., Lu, L., Lajkiewicz, N., Konkol, L.C., Li, Z., Zhang, F., Li, J., Wang, H., Xu, M., et al. (2018). Heterocyclic compounds as immunomodulators, Incyte Corporation, US 2018/0177784 A1.

Zak, K.M., Kitel, R., Przetocka, S., Golik, P., Guzik, K., Musielak, B., Dömling, A., Dubin, G., and Holak, T.A. (2015). Structure of the Complex of Human Programmed Death 1, PD-1, and Its Ligand PD-L1. Structure *23*, 2341–2348.

Zak, K.M., Grudnik, P., Guzik, K., Zieba, B.J., Musielak, B., Domling, A., Dubin, G., and Holak, T.A. (2016). Structural basis for small molecule targeting of the programmed death ligand 1 (PD-L1). Oncotarget *7*, 30323–30335.

Zhou, L., Chong, M.M.W., and Littman, D.R. (2009). Plasticity of CD4+ T Cell Lineage Differentiation. Immunity *30*, 646–655.